Study of the simultaneous Grinding/Ball-burnishing of AISI 4140 based on finite element simulations and experiments

Yasmine Charfeddine, Sawsen Youssef, Salem Sghaier, Jalila Sghaier, Hédi Hamdi

Yasmine Charfeddine, Sawsen Youssef, Salem Sghaier, Jalila Sghaier, Hédi Hamdi. Study of the simultaneous Grinding/Ball-burnishing of AISI 4140 based on finite element simulations and experiments. International Journal of Mechanical Sciences, 2021, 192, pp.106097 -. ⟨10.1016/j.ijmecsci.2020.106097⟩. ⟨hal-03493354⟩

Study of the simultaneous Grinding/Ball-burnishing of AISI 4140 based on finite element simulations and experiments

Yasmine Charfeddine [1, 3,*], Sawsen Youssef [1], Salem Sghaier [1], Jalila Sghaier [2] and Hédi Hamdi [3]

1 University of Monastir, ENIM, LGM, Avenue Ibn El Jazzar, 5019 Monastir- Tunisia; yasmine.charfeddine29@gmail.com; sawsen.youssef@gmail.com; salemsghaier@yahoo.fr
2 University of Monastir, ENIM, LTTPI, Avenue Ibn El Jazzar, 5019 Monastir- Tunisia; jalila.sghaier@enim.rnu.tn
3 University of Lyon, ENISE, LTDS CNRS UMR 5513, 58 rue Jean Parot, 42023 Saint-Etienne – France; hedi.hamdi@enise.fr

*Correspondence: yasmine.charfeddine29@gmail.com; Tel.: +216-92-730-635

Received: date; Accepted: date; Published: date

Abstract: In the manufacturing field, a growing interest is being held to the environment, to sustainability and more precisely saving energy and time. Combining thermomechanical with pure mechanical processes is an eco-friendly and profitable technique. In this paper, it is proposed to combine grinding and ball-burnishing processes. Further from reducing time, energy and cost of the manufacturing operations, this original combination is imagined to take benefit from thermomechanical history occurring while grinding to optimise ball-burnishing process in order to enhance the workpiece surface integrity. In this paper, the impact of this newly developed process on the surface and subsurface behaviour is studied through experiments and 3D FEM simulations. It is shown that performing simultaneously grinding and ball-burnishing processes leads to a thick surface layer up to several millimetres with compressive residual stresses state. This is an interesting result to increase sustainability of metallic workpieces by enhancing wear resistance, fatigue strength and fatigue lifetime.

Keywords: Thermo-mechanical process; Grinding; Ball-burnishing; 3D FEM Simulations; Combined process; Hybrid process; Simultaneous grinding/ball-burnishing

1. Introduction

Grinding process is generally the final operation in the machining process procedure as well as it is often considered as a finishing operation offering high dimensional precision, geometrical shaping accuracy and good surface roughness [1,2]. Nevertheless, this abrasive process can introduce some material deteriorations like microcracks formed at the surface and below the ground zone [3,4] and also burning marks that can appear when reaching high grinding temperature values [5-8]. Some other studies have shown that grinding can lead to scratched and tore surface [9] probably caused by free abrasive grains, pulled off the grinding wheel, in the grinding interface [10–12] or very high workpiece speeds [9]. Moreover, grinding of hardened steel leads to tensile residual stress results at the surface and even beneath it [13,14] that are known to be bad for fatigue resistance [15–19]. Burnishing process is often launched after grinding to fix workpiece deteriorations caused by this thermomechanical abrasive process [20,21].

Burnishing is a purely mechanical process capable of improving surface roughness by pushing into the valleys the microscopic peaks left by the cutting tool on metals by applying a pressure through a burnishing ball or roller. The surface obtained after burnishing has a mirror like finish and is smoother [22–25] and harder [26–30]. Fatigue resistance of mechanical components exposed to cyclic loads is enhanced too [31–35], thanks to the appearance of compressive residual stresses [36,37]. These compressive residual stress results [38] reduce drastically the tensile stress values responsible for the emergence of the cracks and their propagation which enhances fatigue strength. Further, the plastic deformation [39] imposed by the pressure leads to strain hardening which has an impact on the workpiece microstructure [40,41] by refining the material grains beneath the surface [42].

Combining simultaneously grinding with ball-burnishing is a newly developed technique. It consists in grinding and burnishing performing together by placing the burnishing tool on the grinding machine and taking advantages of thermo-mechanical history of the workpiece initiated by the temperature changes occurring while grinding [43,44]. This hybrid manufacturing process ensures obtaining a better surface quality and durability while reducing manufacturing energy and time if compared to grinding and burnishing acting separately.

REGAL (French abbreviation of the combined Grinding Ball-burnishing process) is a promising process since it can enhance surface integrity like the combined turning/burnishing process in terms of surface roughness [45,46], hardness [45,47] and compressive residual stresses obtained on the top surface and subsurface [48]. Such surface integrity improvement increases wear resistance and fatigue life of workpiece. One of the main advantages of this simultaneous grinding/ball-burnishing process is the increase of the affected depth by compressive residual stresses compared to ordinary burnishing process.

The aim of this paper is to present an exploratory research study of the effectiveness of the newly developed technique combining grinding with ball-burnishing process. Researches are carried out by both experimentations and 3D FEM simulations using ABAQUS™/Standard.

2. Materials and experimental set-up

2.1. Materials

The workpiece material considered is the AISI 4140 and its chemical composition and thermo-mechanical behavior properties are resumed subsequently in Table 1 and Table 2. The burnishing ball is made of ceramic and is considered rigid for the rest of the study since its hardness is equal to 75HRC which is more important than the workpiece hardness, equal to 46HRC.

Table 1. Chemical compositions of AISI 4140.

Components	**C**	**Si**	**Mn**	**P**	**S**	**Cr**	**Mo**
Percent (%)	0.41	0.39	0.72	0.025	0.035	1.12	0.27

Table 2. AISI 4140 thermo-mechanical properties.

Young modulus [MPa]	210,000
Poisson's ratio υ	0.3
Density [Kg.m^{-3}]	7800
Thermal conductivity [mW.mm^{-1}.K^{-1}]	46
Specific heat [mJ.t^{-1}.K^{-1}]	477,000,000
Heat change coefficient [W.m^{-2}.K^{-1}]	10^5

2.2. Experimental set-up

The grinding machine used in this study is the ERNAULT-SOMUA FU-500 plane grinder and the burnishing tool used is a hydrostatic Ecoroll HG13 ball-burnishing tool. To make possible the combined grinding and ball-burnishing processes simultaneously, the ball burnishing tool is clamped to the grinding machine head using an aluminum fixing plate (Figure 1). This plate replaces the actual cover of the grinding machine head and it is designed and manufactured to suit the grinding machine used in this study.

The fixing plate is placed on the grinding machine using its two existing nuts and the two clamps on both sides of the grinding machine to guarantee the stiffness of the fixing system on the grinder head. Moreover, the ball-burnishing tool Ecoroll HG13 is placed in the center of the aluminum plate and fastened to it using two U clamps and four nuts and bolts (Figure 1(b)). To ensure grinding and burnishing simultaneously, the ball-burnishing tool is placed vertically in a plane parallel to the grinding wheel disk plane (Figure 1(b)). Further, centers of the contact areas of the grinding wheel and the burnishing ball with the workpiece are in a plane orthogonal to the manufactured workpiece surface containing the wheel center (Figure 1(b)). The "following system" existing in Ecoroll ball burnishing tools guarantees the ball to be always in contact with the ground workpiece.

The performance of grinding and burnishing simultaneously occur when the workpiece is placed under the grinding wheel and the ball-burnishing tool at the same time. The workpiece is then moved forwards and backwards according to a precise cross feed f and at workpiece speed V_w. The grinding machine table is equipped with a KISTLER 9257A force dynamometer to register the resulting forces.

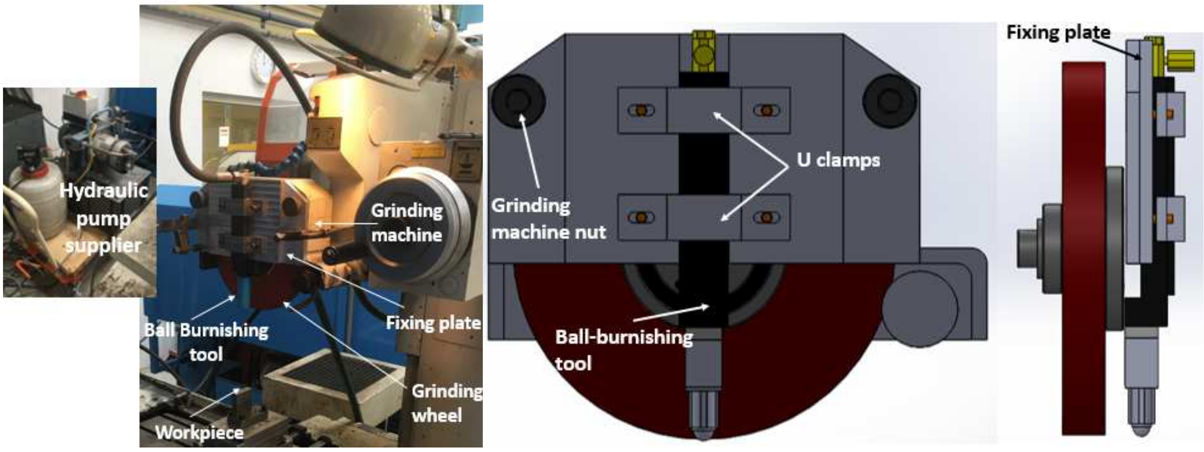

(a) **(b)**

Figure 1. (**a**) Combined grinding/ball-burnishing setup; (**b**) SOLIDWORKS CAD front and side views of the burnishing tool assembly.

The abrasive tool is a type 1 CBN Wendt Boart grinding wheel 250-10-3-B126-RXJ75-76.2. The main dimensions are 250 mm in diameter (D_S), 10 mm in width (b) and 3 mm CBN layer. The burnishing tool used is a hydrostatic Ecoroll HG13 with a ceramic 13 mm diameter burnishing ball controlled using an Ecoroll hydraulic pump supplier (Figure 1(a)). The workpieces are extracted and manufactured from an AISI 4140 bar. The dimensions are 15 mm in width, 50 mm in length and a height of 50 mm.

2.3. Process conditions

The combined grinding/ball-burnishing process conditions are conducted for a workpiece speed of 250 mm.s^{-1}. The other grinding process conditions considered in this study are shown in Table 3 and the other ball-burnishing process conditions are cited in Table 4. P is the set hydraulic pressure supplied by the Ecoroll pump (Figure 1(a)).

Table 3. Grinding conditions.

Peripheral wheel speed	V_s [m.s^{-1}]	37.5
Depth of cut	a_p [µm]	50
Workpiece speed	V_w [mm.s^{-1}]	250

Table 4. Ball-burnishing conditions.

Burnishing ball diameter	d_b [mm]	13
Pressure	P [MPa]	30
Workpiece speed	V_w [mm.s^{-1}]	250
Cross feed	f [mm]	1

3. Modelling and simulation

3.1. Modelling of grinding process

Grinding normal and tangential mechanical forces values are very low and the grinding cutting speeds are very high as compared to other material removing processes such as turning, milling and so on. Nevertheless, grinding power is high due to high grinding speed and it is assumed that all this power is converted as heat [2,6,49]. A fraction of this heat energy goes into the workpiece and involves thermomechanical phenomena because of the loading type, and the strain resulting from the thermal expansion. The rest of energy is dissipated trough out grinding micro-chips and environment.

The grinding process is modeled as a moving heat source representing the action of the abrasive wheel on the workpiece surface (Figure 2). To quantify the input power, it is assumed that all the grinding power is sooner or later converted as heat in the manufacturing area [2,6,49]. Between 65% and 85% of the generated thermal power enter into the workpiece as heat [49–53]. Furthermore, many researchers demonstrated that the heat flux distribution in the grinding area is linearly arranged [43,54]. It is then said that the heat flux is modelled by a triangular moving heat flux [55] along the specimen's surface (Figure 2).

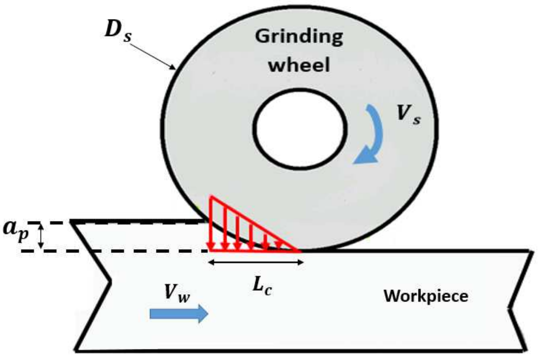

Figure 2. Triangular heat flux distribution.

In this paper the linear heat flux density is computed using Equation 1 as a function of the contact length l_c (Equation 2), the thermal power P_w entering into the workpiece, the active grinding wheel width b, and the curvilinear abscissa Y [43]. The thermal power P_w (Equation 3) is as well depending on the grinding tangential force F_t, the grinding wheel velocity Vs and the fraction ε of the total energy generated that really goes into the workpiece. In this paper, ε is taken equal to 75% [49].

$$q_w(Y)=\frac{2.P_w}{b.l_c^2}.Y;\ Y\in[0,l_c] \quad (1)$$

The contact between the grinding wheel and the workpiece (Figure 2) is defined by an arc circle. The length of this arc is defined as the grinding contact length lc (Equation 2).

$$l_c=\sqrt{a_p.D_s} \quad (2)$$

The thermal power P_w (Equation 3) entering the workpiece is the fraction ε of the total mechanical power generated in the grinding interface. Total mechanical power is the dot product of the grinding force vector by the speed vector that is finally equal to the product of the tangential force component F_t and the peripheral grinding wheel speed V_s.

$$P_w=\mathcal{E}.F_t.V_s \quad (3)$$

The grinding tangential force can be modeled as a function of the equivalent chip thickness h_{eq} considered for the contact surface between the grinding wheel and the workpiece (Equation 4) [43].

$$F_t=20.b.\left(h_{eq}\right)^{0.615} \quad (4)$$

Where:

$$h_{eq}=a_p.\frac{V_w}{V_s} \quad (5)$$

With Equations 1 to 5, it is possible to compute grinding heat flux density that goes into the workpiece (Table 5) for different workpiece speed values and according to the grinding conditions cited in Table 3.

Table 5. Data used to calculate the heat flux densities for different workpiece speed values.

V_w[mm.s^{-1}]	$\frac{2.P_w}{b.l_c^2}$ [W.mm^{-3}]
100	24.3
200	37.26
250	42.74
300	47.81
400	57.1
500	65.46

The heat flux trajectory for numerical simulations of the grinding process are represented in Figure 3. The cross-feed f (Figure 3) is imposed by the ball-burnishing process.

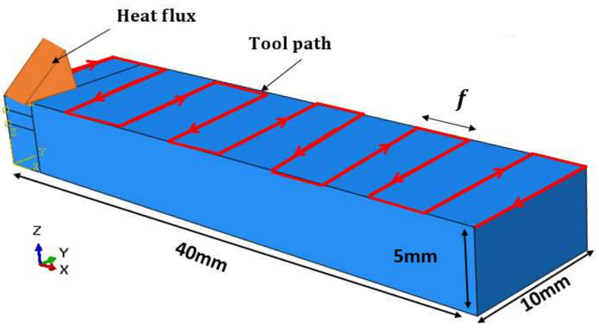

Figure 3. 3D model of step-cross grinding process.

3.2. Ball-burnishing process modelling approaches

The burnishing process can be modelled using two different manners. The first approach consists in using the burnishing force when using the hydrostatic Ecoroll system used in this study (Figure 4(a)). The ball-burnishing force is calculated from the hydraulic pressure P (Figure 4(b)) that is assumed applied on the upper half sphere of the burnishing ball, Equation 6. The other approach consists in applying to the ball the involved vertical displacement δ (Figure 4(a)) resulting from the burnishing force.

$$\mathrm{F_b}{=}\Pi\ \mathrm{R_{ball}^2}\ \mathrm{P} \tag{6}$$

Where: $\mathrm{R_{ball}}$ is the burnishing ball radius.

In the case of the second approach, many research papers, modelled the ball-burnishing process using a burnishing ball controlled by a vertical displacement corresponding to the indentation depth δ (Figure 4(a)) [56, 57] calculated thanks to Hertz theory of contact considered between two elastic solids (Figure 5). The Hertz theory of contact is only valid in the elastic domain whereas burnishing process reaches the plastic domain. For this reason, to study the relevance of using Hertz theory of contact, the calculated value of the vertical displacement δ is compared to the numerical one obtained after indentation taking into account the work hardening.

The computed ball-burnishing force using Equation 6 is different from the real force applied on the 13 mm burnishing ball found experimentally for a set hydraulic pressure P of 30 MPa. This experimental ball-burnishing force measured by a KISTLER 9257A force dynamometer is 25% lower than the calculated force. This can be due to the pressure loss occurring in the gap between the ball and the burnishing tool socket (Figure 4(b)). Then, a new relationship between the calculated and experimental ball-burnishing force is expressed in Equation 7 and is in accordance with literature results [58].

$$\mathrm{F_{b,\,exp}}{=}\ \frac{3}{4}\ \mathrm{F_b} \tag{7}$$

The indentation numerical simulation is then launched using the experimental ball-burnishing force of 2986 N found using Equation 7. The indentation simulation using the experimental burnishing force permits to compare not only the penetration depth δ but also other contact parameters given by Hertz theory of contact.

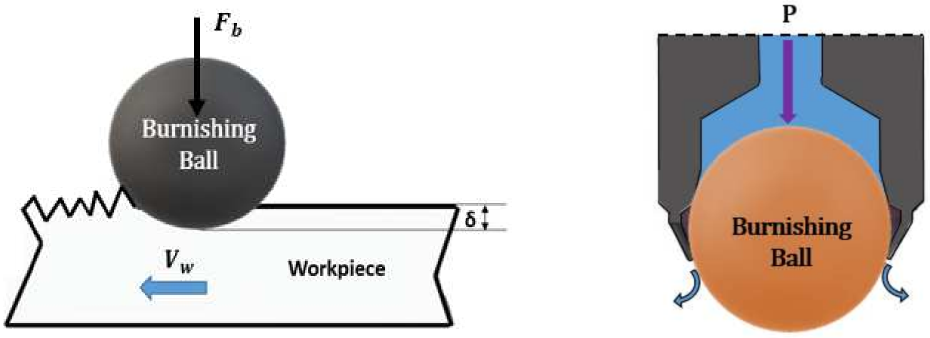

(a) (b)

Figure 4. Ball-burnishing model for (a) an applied ball-burnishing force F_b or an applied vertical displacement δ; (b) Illustration of the burnishing ball and ball retainer.

From Hertz elastic theory between a rigid sphere and a half-space (Figure 5) it is also possible to estimate the contact characteristics between the burnishing ball and the workpiece. One of them is the maximum contact pressure P_0 (Equation 8) between the burnishing ball and the workpiece when ball-burnishing force F_b is applied. Another one is the contact area and the last one is the indentation distance δ of the ball in the part calculated using Equation 9.

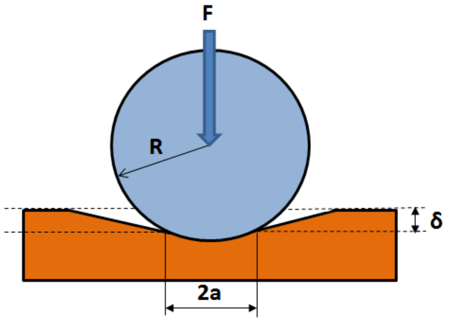

Figure 5. Illustration of Hertz elastic theory of contact.

The circular contact area diameter 2a is calculated using Equation 10, knowing that E^* (Equation 11) is the effective modulus, and R is the effective radius (Equation 12).

$$P_0=\frac{3\ F_b}{2\ \Pi\ a^2} \tag{8}$$

$$\delta=\frac{a^2}{R_{ball}} \tag{9}$$

$$2a=2\left(\frac{3\ F_b\ R}{4E^*}\right)^{\frac{1}{3}} \tag{10}$$

$$E^*=\left(\frac{1-\upsilon_{workpiece}{}^2}{E_{workpiece}}+\frac{1-\upsilon_{ball}{}^2}{E_{ball}}\right)^{-1} \tag{11}$$

$$\frac{1}{R}=\left(\frac{1}{R_{workpiece}}+\frac{1}{R_{ball}}\right) \tag{12}$$

The contact material properties of the workpiece and the burnishing ball used in this study are cited in Table 6.

Table 6. Mechanical and geometric properties related to Hertzian contact calculation.

$E_{workpiece}$ [MPa]	E_{ball} [MPa]	$\upsilon_{workpiece}$	υ_{ball}	E^* [MPa]	$R_{workpiece}$ [mm]	R_{ball} [mm]	R [mm]
210,000	315,000	0.3	0.26	137,111	∞	6.5	6.5

The calculated Hertzian parameters for a pressure value of 30 MPa are presented in Table 7.

Table 7. Calculated Hertzian parameters for an applied hydraulic pressure of 30 MPa.

P [MPa]	F_b [N]	2a [mm]	P_0 [MPa]	δ [mm]
30	3,982	1.04	6,999	0.042

The maximum indentation depth δ obtained numerically in Figure 6(a) is equal to 0.029 mm and is 15% lower than the calculated value using Hertz theory of contact that is equal to 0.034 mm. In addition, the contact area diameter 2a found numerically in Figure 6(b) is equal to the calculated Hertzian value given in Table 8 and equal to 0.95 mm. In the other hand, Hertz theory of contact maximizes the contact pressure results P_0 equal to 6359 MPa calculated using Equation 8 as it is equal to 2456 MPa for the numerical simulations of indentation in Figure **7**(a) and Figure 7(b). This difference can be explained by the fact that Hertz theory of contact is only valid in the elastic contact hypothesis and does not take into consideration the plastic deformation occurring.

From this comparative study, it is clear that the determination of the penetration depth δ by Hertz theory of contact is a poor approximation to simulate the burnishing process since it is overestimated by 15%. Using such penetration depth δ in burnishing process simulations involve an overestimation of the residual stress results obtained by burnishing.

To avoid further singularities related to the use of Hertz elastic theory of contact, the numerical simulations of the ball-burnishing process in this work are conducted using the experimental ball-burnishing force $F_{b,\ exp}$ instead of using the depth of penetration calculated using Hertz theory of elastic contact.

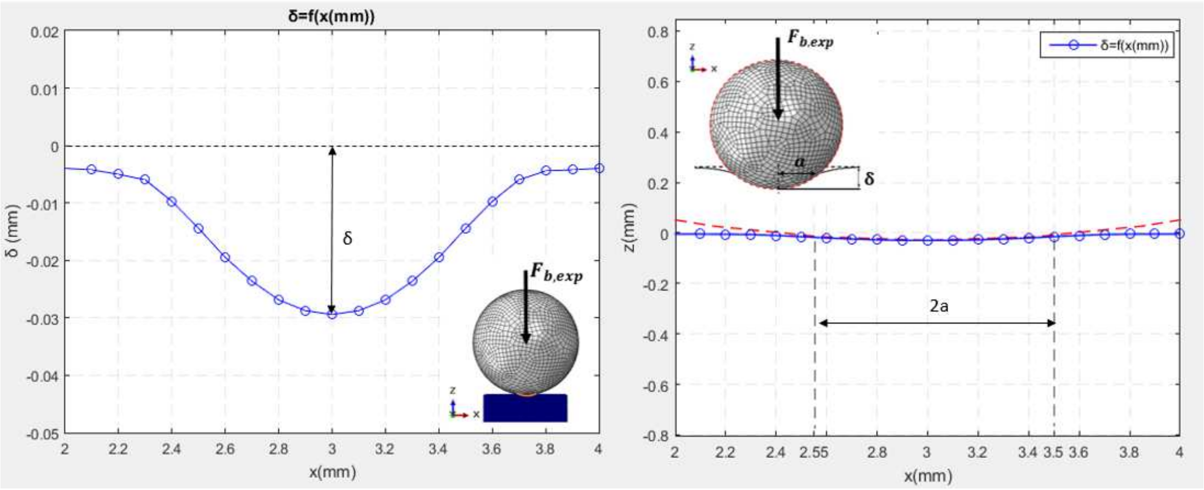

(a) **(b)**

Figure 6. Numerical results of indentation using $F_{b,\ exp}$: (a) Indentation depth δ; (b) circular contact area diameter between the burnishing ball and the workpiece.

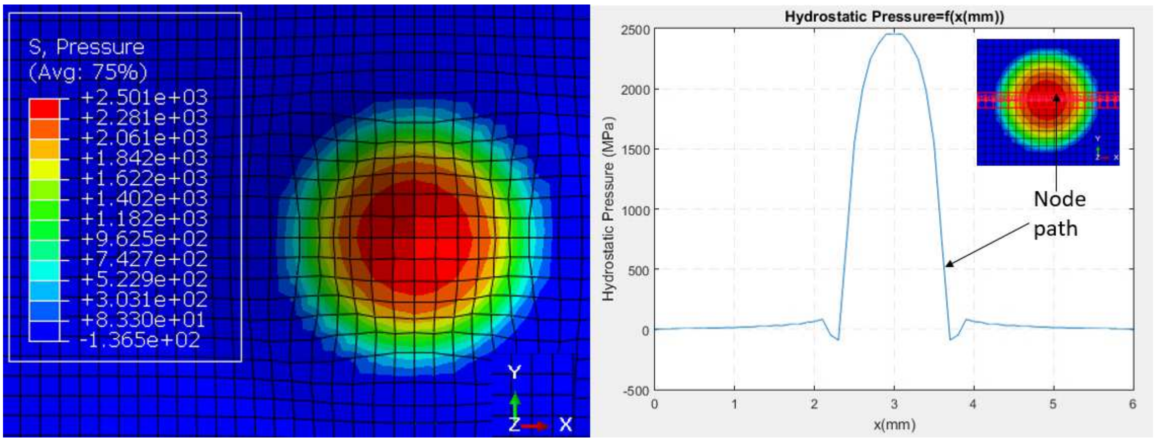

(a) **(b)**

Figure 7. (a) Numerical hydrostatic pressure results after indentation; (b) Hydrostatic pressure curve along X-axis.

Table 8. Calculated Hertzian parameters versus numerical results after indentation for an applied ball-burnishing force of 2986 N.

	$F_{b,\,exp}$ [N]	δ [mm]	2a [mm]	P_0 [MPa]
Hertz theory	2,986	0.034	0.95	6,359
FEM Analysis	2,986	0.029	0.95	2,456

3.3. Adopted approach for modelling ball-burnishing process

In the previous section, it has been demonstrated that using Hertz elastic theory of contact is not adequate for the burnishing process since it does not take into account the work hardening occurring while burnishing. The best way to model burnishing process is either to launch an indentation study using the experimental burnishing force and taking into consideration plasticity and then simulate the burnishing process using the value of the vertical displacement found numerically or directly simulate the burnishing process using the experimental burnishing force. In this study, the burnishing simulation adopted is using an applied experimental burnishing force to avoid supplementary time by using two simulations instead of one.

The ball-burnishing process is modeled by a rigid ball rolling on the workpiece surface at the workpiece velocity V_w and on which an experimental burnishing force $F_{b,exp}$ is applied at its center (Figure 8).

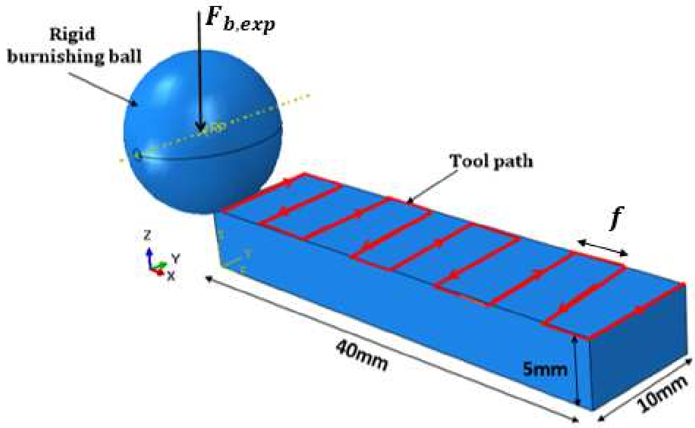

Figure 8. Ball-burnishing model.

3.4. Modelling of combined grinding/ball-burnishing process

The combined grinding/ball-burnishing process model consists in placing the burnishing ball next to the triangular heat flux. The burnishing ball and the heat flux move forwards and backwards along a predefined path and at the same speed equal to the workpiece speed V_w (Figure 3 and Figure 9).

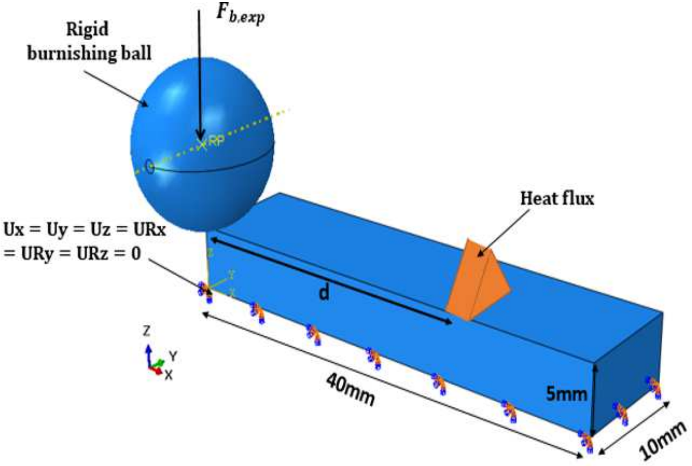

Figure 9. Combined grinding/ball-burnishing model**.**

The 3D model of combined grinding/ball-burnishing is considered thanks to the software ABAQUS™/Standard. The implicit method of calculation is then chosen to simulate especially material spring back in order to obtain the simulated residual stress.

Only a part of the experimental specimen with the dimensions of 40x10x5 mm^3 (Figure 9) was considered in the numerical simulation in order to optimize the geometrical model and to reduce simulations time. The workpiece is considered deformable with a Johnson-Cook elasto-plastic constitutive law and is fixed at its bottom.

The Johnson-cook parameters used in this study for the AISI 4140 are in Table 9.

Table 9. Johnson-cook parameters for the AISI 4140 [59].

A[MPa]	B[MPa]	n	m
595	580	0.133	1.03

Where: A is the yield stress (MPa), B the hardening modulus (MPa), n is the work hardening exponent and m the thermal softening coefficient.

Grinding is modeled by a moving heat flux along the workpiece surface following a step-cross path (Figure 3). The shape distribution of the heat flux is considered triangular in the grinding working interface where the initial workpiece temperature is 20°C and the convective heat exchange coefficient is equal to 10^5 $W.m^{-2}.K^{-1}$. Whereas, the ball-burnishing process is modeled by a rigid ball free to rotate along the workpiece surface with an imposed vertical force (along Z direction) applied to its center (Figure 9) and calculated using Equation 7. The value of the ball-burnishing force applied to the burnishing ball considered for the ball-burnishing conditions presented in Table 4 equal to 2986 N is validated thanks to the normal experimental force obtained in the stabilized zone (Figure 10(b)).

The simulation of the ball-burnishing process is composed of three steps: indentation, rolling and disengagement. The ball-burnishing boundary conditions vary according to the actual step used along the study and are summarized in Table 10.

Table 10. Boundary conditions of the burnishing ball.

Step	**U1**	**U2**	**U3**	**UR1**	**UR2**	**UR3**	**Force**
Indentation	0	0	free	0	0	0	$F_{b,\ exp}$
Rolling	*	*	free	free	free	free	$F_{b,\ exp}$
Disengagement	0	0	2 mm	0	0	0	0

* depends on the actual position of the ball along X and Y directions according to the predefined trajectory.

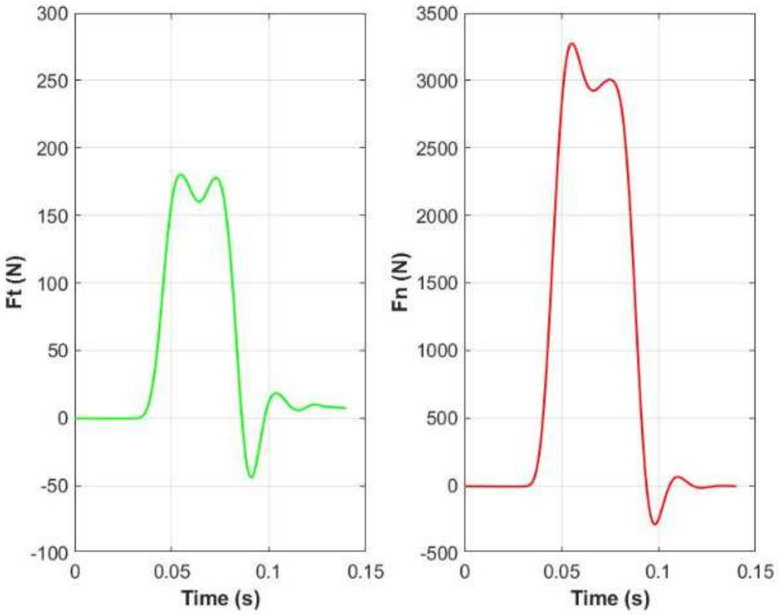

(a) **(b)**

Figure 10. (a) Experimental ball-burnishing tangential force results; (b) Experimental ball-burnishing normal force results.

In order to estimate the right numerical coulomb friction coefficient proper to the ball-burnishing process, finite element residual stress results obtained for different friction coefficient are compared to the experimental residual stress results. The dynamic friction force F_t is composed of an adhesive force $F_{t,a}$ and a force related to the plastic deformation $F_{t,d}$ given by the Equation 13 [60].

$$F_t = F_{t,a} + F_{t,d} = (\mu_a + \mu_d) F_n \tag{13}$$

Where: $\mu_a$is the adhesive friction coefficient and μ_d is the deformation friction coefficient.

The ABAQUS software permits introducing the Coulomb friction coefficient proper to purely friction. The Coulomb friction law becomes a poor approximation since there is an adhesive friction that needs to be considered. The friction coefficient obtained experimentally μ_{exp} includes the adhesive μ_a and deformation friction coefficient μ_d expressed in Equation 14. Therefore, from the numerical simulation it is possible to guess the adhesive coefficient by inserting the right coulomb friction value. To determine the adhesive coefficient, the coulomb friction coefficient is changed until obtaining similar experimental and numerical residual stress curves.

$$\mu_{exp}=\frac{F_t}{F_n}=(\mu_a+\mu_d) \tag{14}$$

Considering the experimental ball-burnishing force results given in Figure 10(a) and Figure 10(b), the calculated force ratio between the tangential ball-burnishing force F_t and the normal ball-burnishing force F_n mean values is equal to 0.06 which is the experimental value of the friction coefficient calculated in the stabilized zone.

Combined grinding/ball-burnishing is a thermo-mechanical study so the mesh considered is type C3D8T. A refined mesh is adopted for a part of the workpiece (3x10x5 mm^3) which is the interest zone presented in Figure 11. This precision of the mesh was chosen to see clearly the impact of this newly developed technique beneath the workpiece surface and reduce the calculation time by not considering a refined mesh for the total workpiece.

A study of mesh convergence of the workpiece was launched where different mesh sizes were considered (Figure 11). The choice of the adequate workpiece mesh was adopted based on two criteria. First criterion is that the mesh size along X-axis has to be lower than the cross feed f (1 mm) and the mesh size according to Y-axis has to be lower than the contact length between the workpiece and the grinding wheel lc (3.5 mm) and at the same time lower than the contact area diameter between the burnishing ball and the workpiece 2a (0.95 mm). The second criterion is the report CPU time (Table 11).

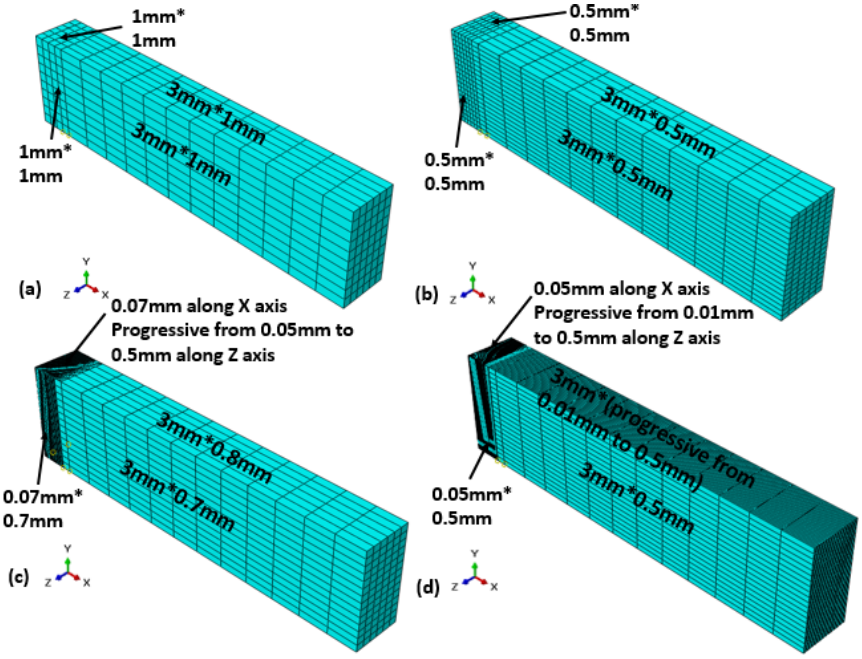

Figure 11. Different workpiece mesh: (a) coarse mesh; (b) normal mesh; (c) optimal mesh; (d) very fine mesh.

Table 11. Mesh strategy versus CPU time.

Mesh strategy	Illustration	CPU time
Coarse mesh size in the interest zone	Figure 11(a)	1 day
Normal mesh size in the interest zone	Figure 11(b)	3 days

Finer mesh size in the interest zone	Figure 11(c)	1 week
Very fine mesh size in the interest zone	Figure 11(d)	More than 2 weeks

The mesh strategy adopted in Figure 11(a) does not obey to the first criterion and the mesh strategy adopted in Figure 11(b) gave results with a lack of precision if compared to results obtained for the mesh strategy in Figure 11(c) and Figure 11(d). Further, no noticeable changes in the output data are registered between the mesh strategy in Figure 11(c) and Figure 11(d) except time CPU that is higher (Table 11).

Since the precision of the results given by workpiece mesh in Figure 11(c) and Figure 11(d) are close, the adopted mesh in this study is the one illustrated the in Figure 11(c) with a total of 26,962 elements and 30,058 nodes (Figure 12). This chosen mesh strategy permits to gain in simulation time and ensures convergence of the model.

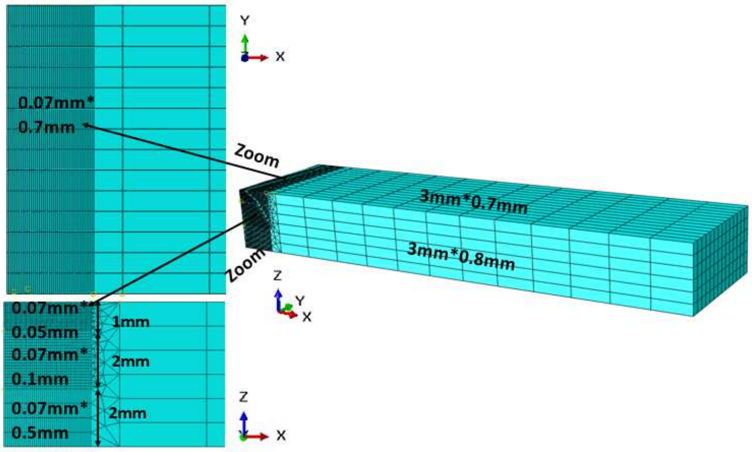

Figure 12. Adopted workpiece mesh.

3.5. Results

Simultaneous combined grinding/ball-burnishing consists in burnishing a pre-heated surface by the grinding process. The effect of grinding temperature results is studied numerically for different workpiece speeds V_w and cross feed values f (Figure 13 and Figure 14). The purpose behind this study is to maximize temperature results reached at the surface and beneath it while burnishing. The temperature results according to the depth of the workpiece are studied to optimize the grinding temperatures and choose the adequate grinding parameters to consider in the combined grinding/ball-burnishing process.

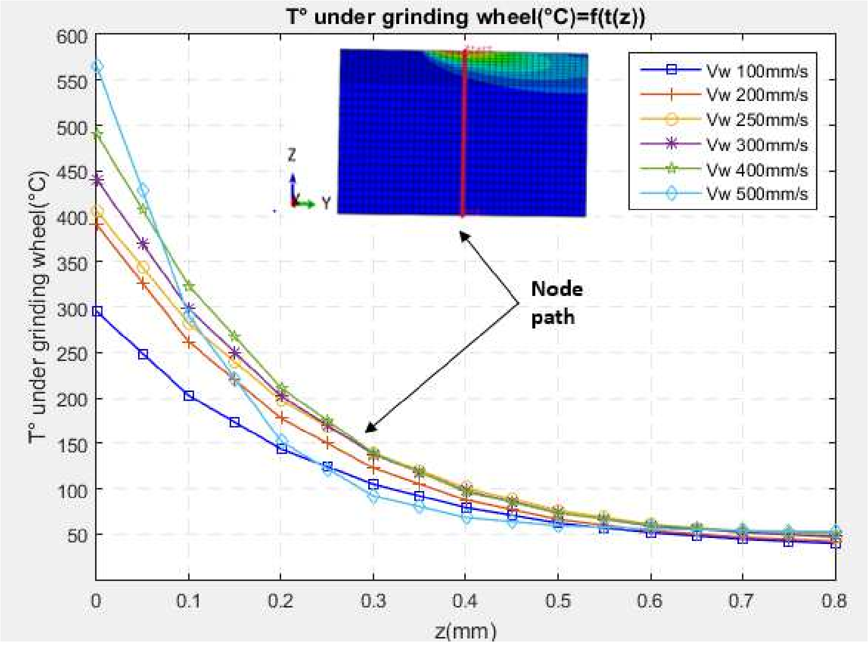

Figure 13. Effect of the workpiece speed on the numerical grinding temperature results along the workpiece depth for a cross feed of f=0.25 mm.

The highest temperature result at the workpiece surface is obtained for V_w=500 mm.s^{-1} and is equal to 565°C and the lowest equal to 295°C is obtained for V_w=100 mm.s^{-1} shown (Figure 13). The temperature of the workpiece surface increases when the workpiece speed increases. The more the workpiece speed increases, the more the heat flux density values increase, the more the temperature obtained at the surface are high.

Regardless of the cross-feed variations, the same heat flux densities ae obtained since the cutting parameters (a_p,V_w,V_s) and the contact length l_c didn't change. When the cross-feed increases, the contact surface S_c=f.l_c increases which leads to higher thermal power entering the workpiece which explains obtaining higher temperature results. As the surface of contact between the heat flux and the workpiece is the greatest for a cross-feed f=1 mm, the maximum temperature of about 470°C is then reached at the top surface (Figure 14).

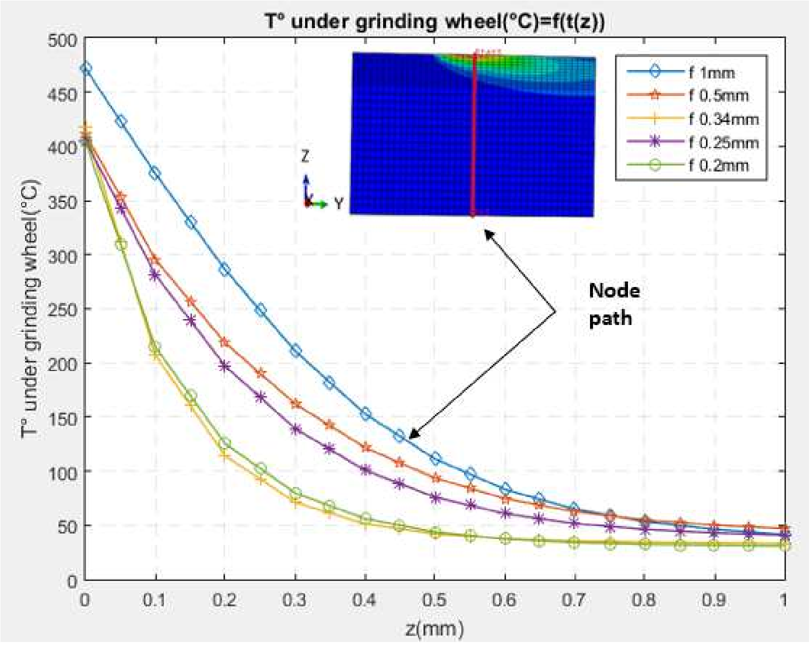

Figure 14. Effect of the cross feed on the numerical grinding temperature results along the workpiece depth for V_w=250 $mm.s^{-1}$ and $q_w(Y)$=42.74.$Y\ W.mm^{-2}$.

The grinding heat flux affects not only the workpiece surface, but heat generated also diffuses in the workpiece core, and leads to high temperature gradients up to different workpiece depths (Figure 13 and Figure 14). The temperature values reach 150°C at a depth of 0.4 mm of the workpiece for a cross-feed of 1 mm and V_w=250 mm.s^{-1} (Figure 14).

For the following numerical and experimental study of the combined grinding/ball-burnishing process, the experiments are launched at a workpiece speed of V_w=250 mm.s^{-1} and a cross feed of f=1 mm where high temperature values are reached while grinding.

After grinding, tensile residual stress are obtained in the grinding direction S22 and perpendicular to grinding direction S11 (Figure 15). These tensile residual stress results are known to be bad for the workpiece lifetime, wear and corrosion resistance since they are responsible for the emergence and propagation of fatigue cracks [61].

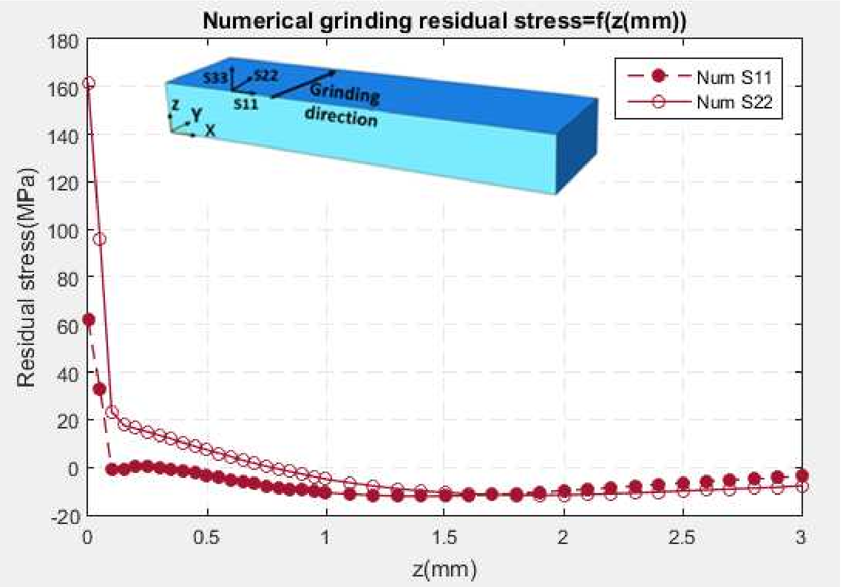

Figure 15. Numerical grinding residual stress results along the workpiece depth for a cross feed of f= 1 mm, V_w=250 mm.s^{-1} and $q_w(Y) = 42.74\, Y\, W.mm^{-2}$.

The modelling approach adopted for the ball-burnishing process has an impact on the residual stress obtained. As mentioned earlier in the modelling of ball-burnishing process section 3.2, two ways of modelling the ball-burnishing process are possible either applying a vertical displacement δ=0.034 mm calculated using Hertz theory of contact or applying the experimental value of the ball-burnishing force $F_{b,\,exp}$ =2986 N to the burnishing ball (Table 8). When comparing numerical residual stress obtained for those two types of modelling it is clear that there is a significant difference. The residual stress results are more compressive in the burnishing direction S22 for the imposed δ compared to the residual stress results obtained for an imposed ball-burnishing force (Figure 16). These compressive residual stress results in the burnishing direction S22 reach a value of -257 MPa at the surface and a maximum compressive value of -578 MPa at a 0.3 mm depth whereas the maximum value of the compressive residual stress result obtained when a ball-burnishing force is applied are equal to -147 MPa obtained at the top surface (Figure 16). Residual stress computed in the perpendicular to burnishing direction S11 are more compressive at the surface equal to -693 MPa when applying a ball-burnishing force, as they are equal to -412 MPa when imposing a vertical displacement to the burnishing ball (Figure 17). Moreover, the compressive residual stress layer reaches a more important depth equal to 0.65 mm when imposing a vertical displacement δ than when applying a ball-burnishing force with an affected depth of 0.5 mm (Figure 16). This can be explained by the fact that the indentation depth δ considered as vertical displacement calculated with Hertz theory of contact equal to 0.034 mm is higher than the indentation depth found numerically when imposing a ball-burnishing force equal to 0.029 mm (Figure 6(a)). Thus, higher indentation depth leads to higher compressive residual stress results at a more important workpiece depth.

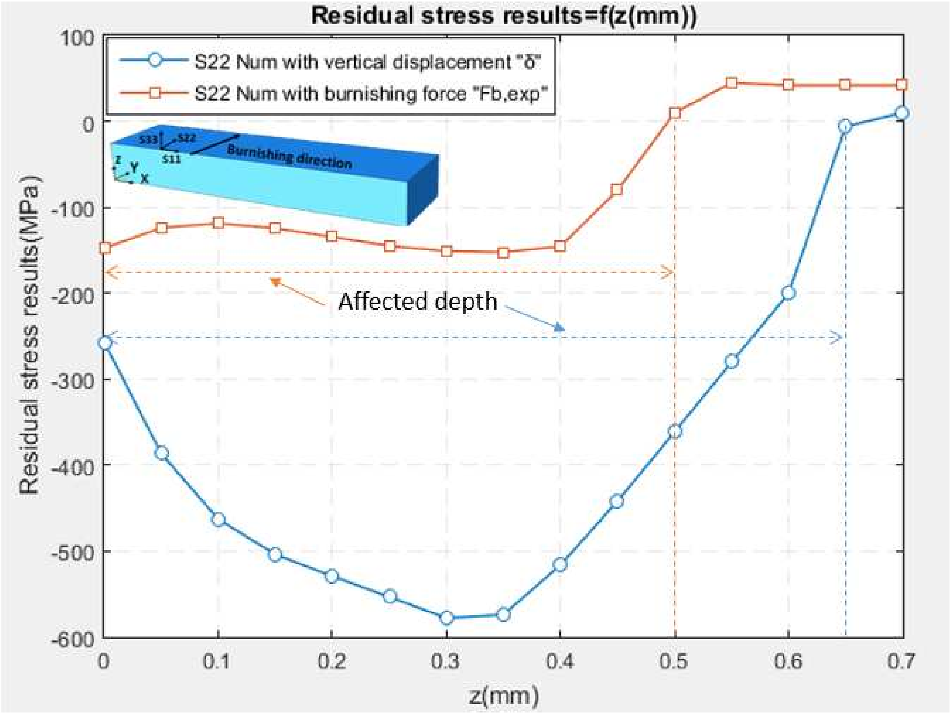

Figure 16. Numerical ball-burnishing residual stress results in the burnishing direction S22 along the workpiece depth for an applied vertical displacement δ=0.034 mm and a numerical ball-burnishing force $F_{b,\,exp}$=2986 N for μ=0.06.

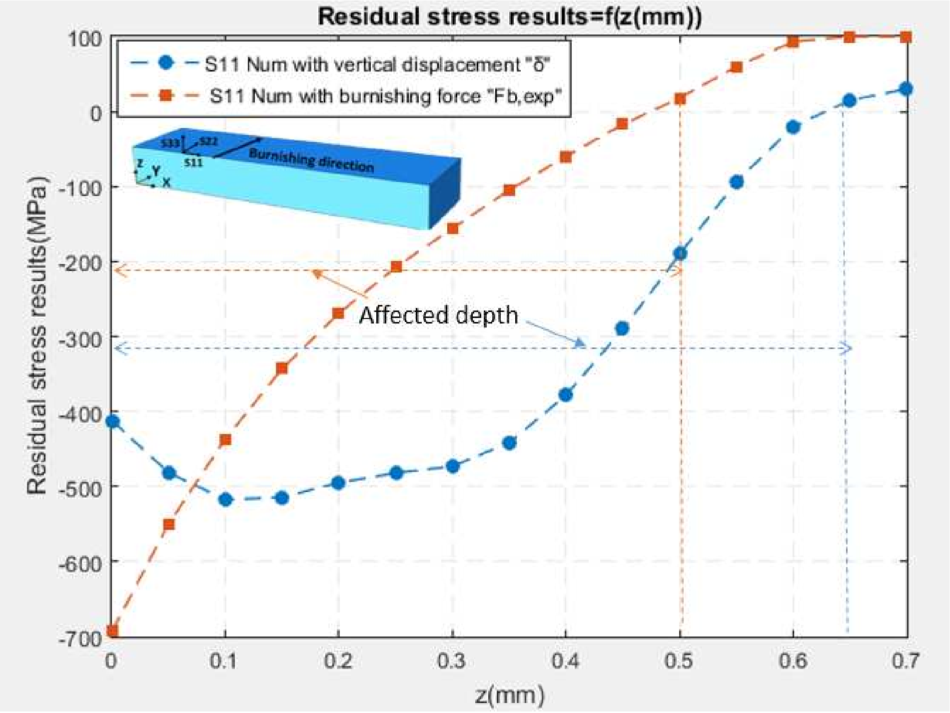

Figure 17. Numerical ball-burnishing residual stress results perpendicular to burnishing direction S11 along the workpiece depth for an applied vertical displacement δ=0.034 mm and a numerical ball-burnishing force $F_{b,\,exp}$=2986 N for μ=0.06.

Residual stress results obtained experimentally for the combined grinding/ball-burnishing process are compared to the numerical results obtained for both modelling approaches used to model the ball-burnishing process (Figure 18 and Figure 19). Residual stress results are more compressive at the top surface when numerical vertical displacement is adopted. These residual stresses can reach a value of -863 MPa in the perpendicular to grinding and burnishing direction S11 (Figure 18) and -311 MPa in the grinding and burnishing direction S22 (Figure 19). But residual stress profile at the top surface and beneath it for S11 and S22 when applying a ball-burnishing force are closer to the experimental results of the combined grinding/ball-burnishing. This led to the use of the imposed ball-burnishing force for the numerical simulation of ball-burnishing in the combined grinding/ball-burnishing process.

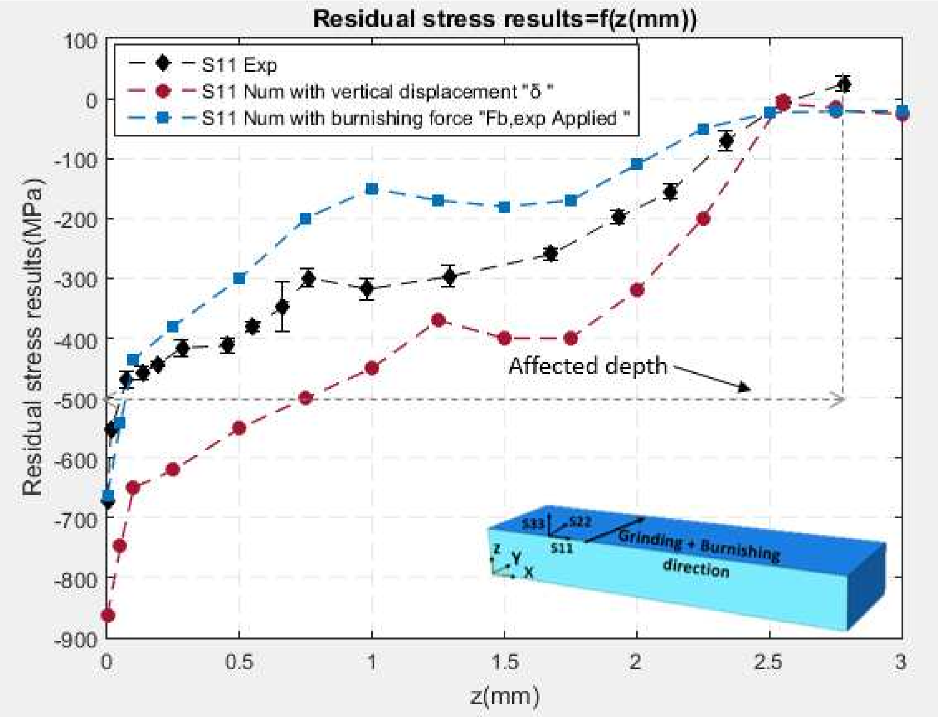

Figure 18. Comparison between experimental and numerical REGAL residual stress results S11 (perpendicular to burnishing and grinding direction) using an applied vertical displacement δ=0.034 mm and a numerical ball-burnishing force $F_{b,\ exp}$=2986 N and μ=0.06.

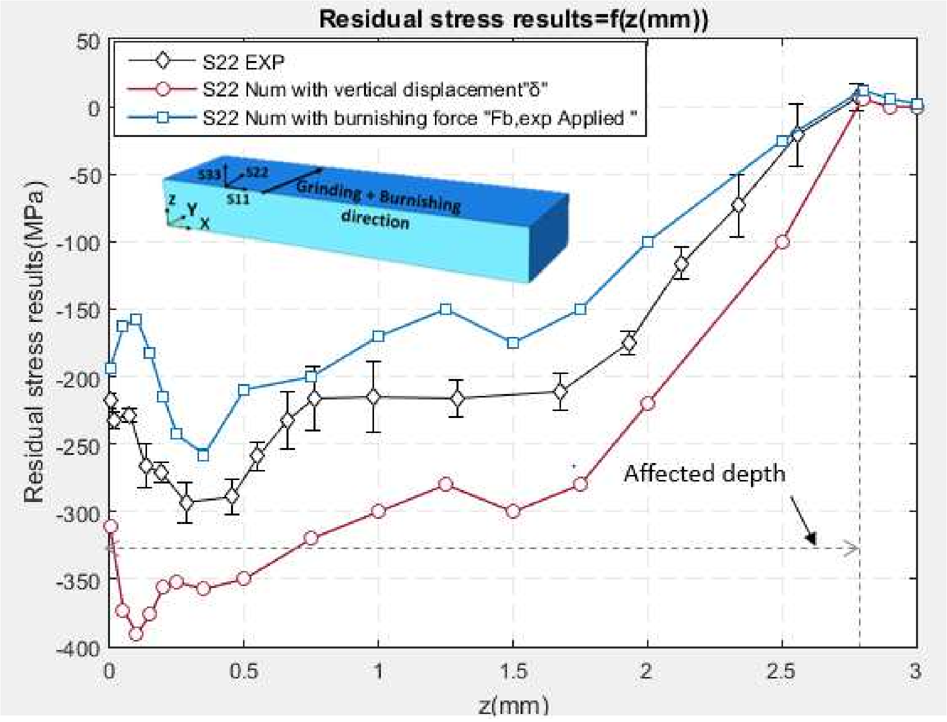

Figure 19. Comparison between experimental and numerical REGAL residual stress results S22 (in the burnishing and grinding direction) using an applied vertical displacement δ=0.034 mm and a numerical ball-burnishing force $F_{b,\ exp}$=2986 N and μ=0.06.

Different Coulomb friction coefficient values of μ=0.03, 0.04, 0.05 and 0.06 where considered in the numerical simulation of the REGAL process using an imposed experimental ball-burnishing force applied to the burnishing ball modelling approach.

Residual stress results obtained numerically in the grinding and burnishing direction (S22) and perpendicular to them (S11) are compressive and in agreement qualitatively with the experimental curve obtained for the same operating conditions (Figure 20 and Figure 21). Furthermore, the same affected depth by the combined grinding/ball-burnishing equal to 2.7 mm is obtained numerically and experimentally (Figure 20 and Figure 21). Maximum compressive residual stress results are obtained at the surface and decrease gradually beneath it according to the perpendicular direction to grinding and burnishing S11 (Figure 20). Whereas in the grinding and burnishing direction S22, the compressive residual stress results increase gradually in the subsurface until reaching a certain depth equal to 0.35 mm (Figure 21).

Residual stress profiles obtained numerically for several friction coefficients are perfectly superimposed on each other in the direction that is perpendicular to burnishing S11 (Figure 20). Residual stress profiles in the grinding and burnishing direction S22 are slightly different for the four different friction coefficients and only for the first 0.75 mm depth of the specimen (Figure 21). These curves deviations are compared to experimental residual stress profiles (Figure 20 and Figure 21). At the surface, the residual stress results in the burnishing direction S22 for the friction coefficient values of 0.04, 0.05 and 0.06 are equal to -197 MPa. However, for a friction coefficient of 0.03, the residual stress value at the surface is equal to the experimental value of -218 MPa. Knowing that the force ratio between the tangential force F_t and the normal force F_n (Figure 10) is equal to 0.06. The approximation of the adhesive coefficient is then possible using Equation 14. Thanks to the adequacy between the experimental and numerical curve obtained for a friction coefficient of 0.03, the adhesive coefficient is then equal to 0.03.

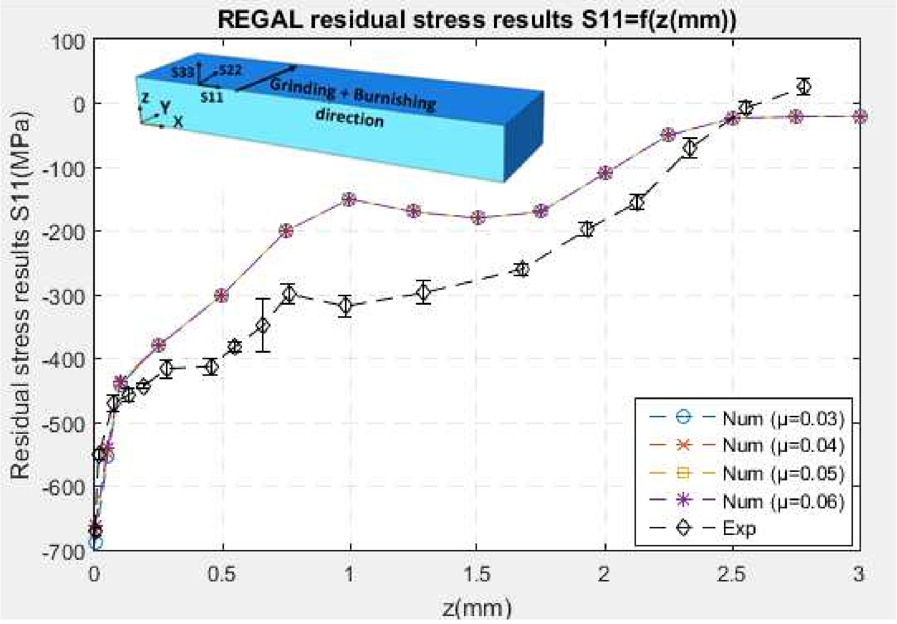

Figure 20. Comparison between numerical and experimental REGAL residual stress results S11 (perpendicular to the grinding/ball-burnishing direction) along the workpice depth for different friction coefficient values, a cross feed of f=1 mm, V_w=250 mm.s^{-1} and $F_{b,\,exp}$=2986 N.

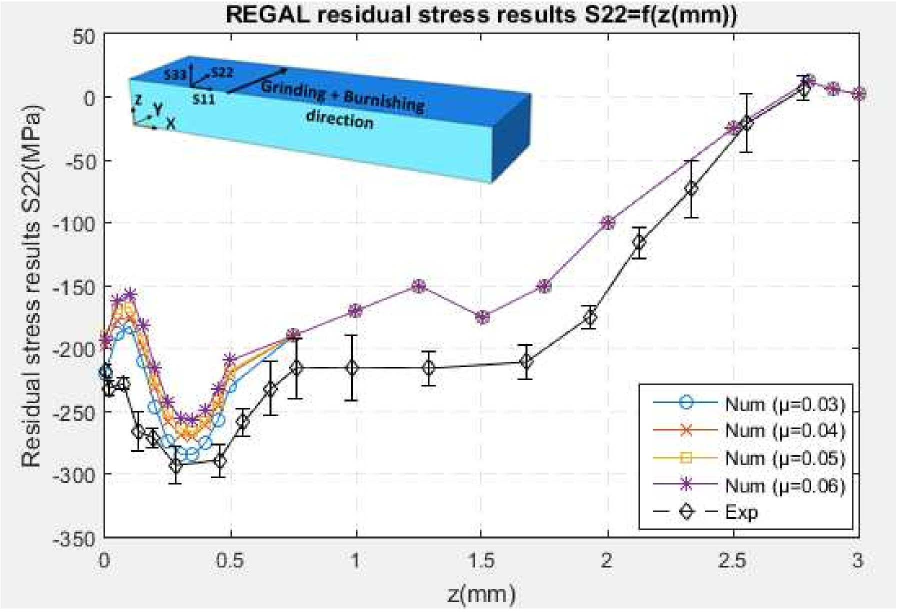

Figure 21. Comparison between experimental and numerical REGAL residual stress results S22 (in the grinding/ball-burnishing direction) along the workpiece depth for different friction coefficient values, a cross feed of f=1 mm, V_w=250 mm.s^{-1} and $F_{b,\ exp}$=2986 N.

In order to analyze the effect of the newly developed technique involving grinding and ball-burnishing acting simultaneously, the residual stress results obtained by FE simulations are compared to those obtained numerically for grinding and ball-burnishing acting separately (Figure 22 and Figure 23). From these figures, it is seen that combining grinding with burnishing converts the tensile residual stresses obtained after grinding into compressive ones. These tensile residual stress results are equal to 161 MPa in the grinding direction S22 (Figure 23) and 62 MPa for the perpendicular to grinding direction S11 (Figure 22). The compressive residual stresses in perpendicular to grinding and burnishing direction S11 obtained at the surface reach values up to -693 MPa (Figure 22) for both REGAL and ball-burnishing process. On the other hand, REGAL process increases the compressive residual stresses results in the grinding and burnishing direction S22 if compared to the stress results obtained after the ball-burnishing process acting separately. Indeed, the compressive residual stress results at the surface increased from-147 MPa for the conventional ball-burnishing to -218 MPa for the combined grinding/ball-burnishing process (Figure 23). This can be interpreted by the fact that more mechanical working is induced when combing grinding with ball-burnishing process. Knowing that two mechanical loadings are involved in REGAL process one related to the thermo-mechanical loading relative to the grinding wheel and the other to the force applied to the burnishing ball.

The affected depth by the compressive residual stress results is more important for the combined process reaching 2.7 mm as it is only 0.5 mm for the regular ball-burnishing process (Figure 22 and Figure 23). This can be explained by the fact that in REGAL process, it seems that grinding temperature may activate for a sufficient duration a decrease of the mechanical behavior optimizing the ball-burnishing process leading to a deeper affected surface layer. The association of high temperature with high burnishing pressure leads to more mechanical working, which enhances compressive residual stress results at a more affected depth.

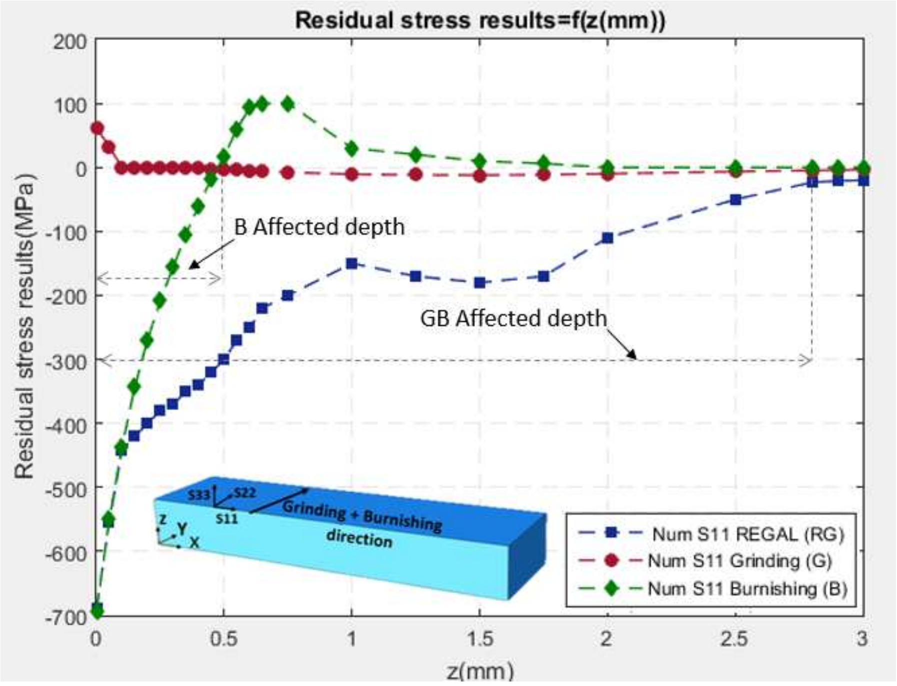

Figure 22. Numerical residual stress results S11 (perpendicular to the grinding/ball-burnishing direction) along the workpiece depth obtained for grinding (G), burnishing (B) and combined grinding/ball-burnishing (GB).

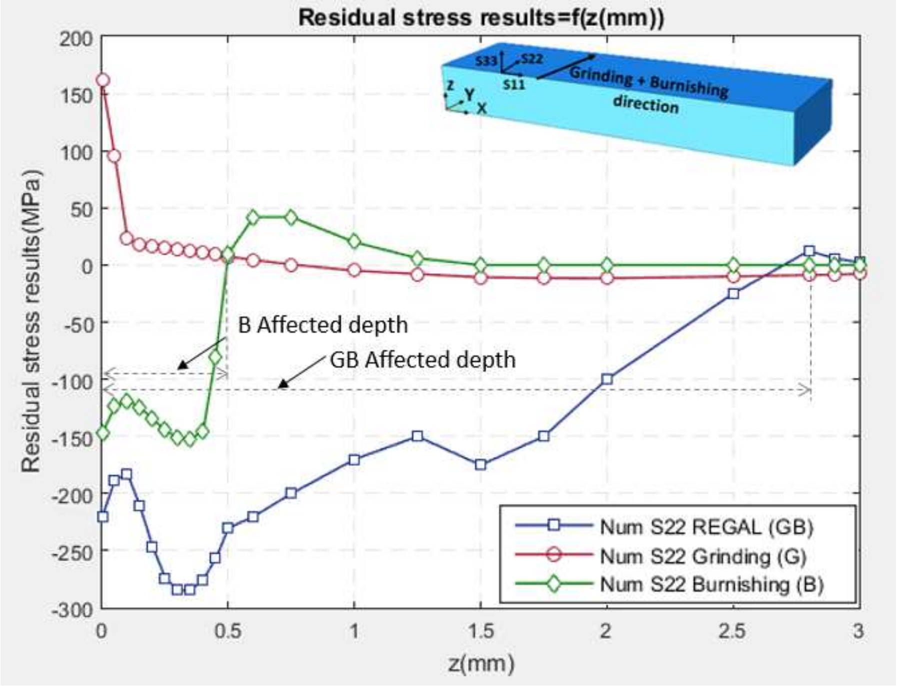

Figure 23. Numerical residual stress results S22 (in the grinding/ball-burnishing direction) along the workpiece depth obtained for grinding (G), burnishing (B) and combined grinding/ball-burnishing (GB).

To see the impact of the burnishing pressures on the residual stress state and the compressive affected depth by the combined grinding/ball-burnishing process, five different supply pressures were considered in the numerical study: 10 MPa, 22.5 MPa, 30 MPa, 32.5 MPa and 35 MPa (Figure 24 and Figure 25). At the surface, the maximum compressive residual stress results are obtained for the maximum pressure of 35 MPa (Figure 24 and Figure 25) reaching a value of -934 MPa for S11 and -310 MPa for S22. Higher pressure values generate more compressive residual stress at the surface and beneath it and a more important compressive affected layer depth as reflected for the residual stress results S11 (Figure 24). This would be the results of the increase in the burnishing ball penetration depth related to the increase of the ball-burnishing force applied to the rolling burnishing ball.

Tensile residual stress results in the burnishing direction S22 equal to 36 MPa are obtained for a pressure of 10 MPa (Figure 25). This can be explained by the fact that this pressure might not be sufficient to convert the grinding tensile residual stress results into compressive ones.

The affected depth by the combined grinding/ball-burnishing process is the same for the pressure values of 22.5 MPa, 30 MPa, 32.5 MPa and 35 MPa equal to 2.7 mm but this depth is equal to 1.75 mm for a pressure of 10 MPa (Figure 24 and Figure 25). According to these numerical results, the more the pressure increases, the more the affected depth increases but not infinitely since it is stabilized at 2.7 mm for a pressure of 22.5 MPa.

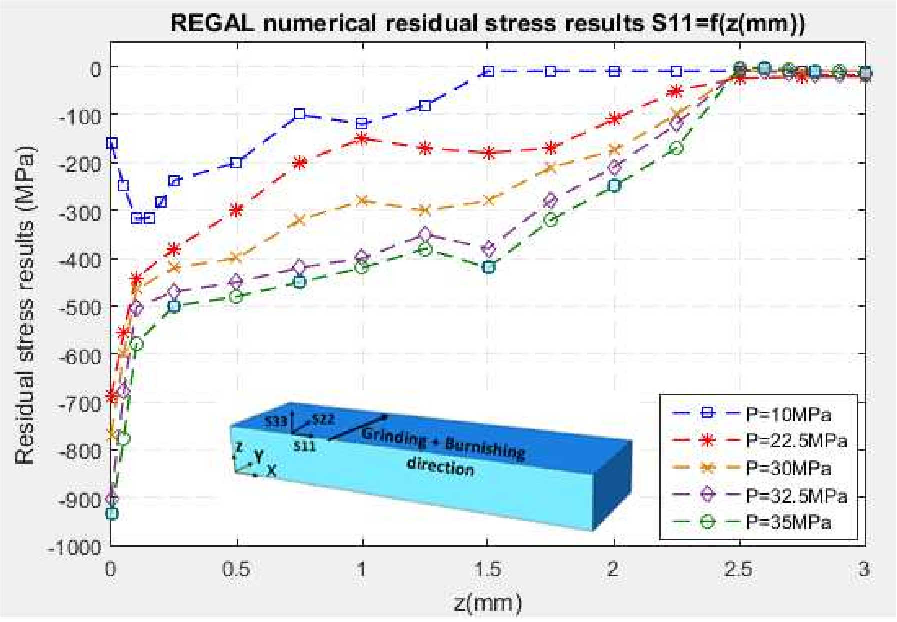

Figure 24. Impact of the burnishing pressure (P) on the numerical residual stress results S11 perpendicular to grinding/ball-burnishing direction along the workpiece depth.

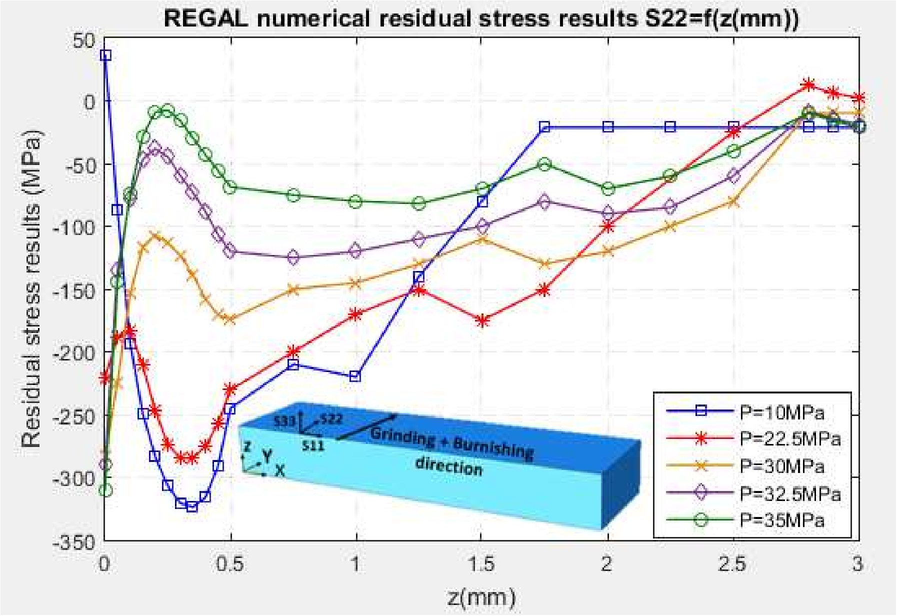

Figure 25. Impact of the burnishing pressure (P) on the numerical residual stress results S22 in the grinding/ball-burnishing direction along the workpiece depth.

Higher burnishing pressures lead to more compressive residual stress results at the surface and reach a more important affected layer. This can be explained according to Revankar et al. [62] that the increase of the ball-burnishing force applied to the burnishing ball leads to an increase in the amount of plastic deformations involved and enhance the hardness of the workpiece at an important workpiece depth.

Indeed, the temperature change under the ground surface and the plastic deformation occurring with ball-burnishing acting simultaneously increase the depth of the plastically deformed layer. The more the burnished depth increase the more the strain hardening increase. Since while ball-burnishing, the material is deformed at a constant volume and the surface deformation leads to its hardening which affects its subsurface by the same material strain hardening circle.

The study of the effect of the pressure on the residual stress results leads to knowing that there is a certain threshold value of the pressure. Starting from this pressure value, the affected workpiece depth by the combined grinding/ball-burnishing process does not increase and is stable for the current process manufacturing conditions to 2.7 mm.

Further, simultaneous grinding/ball-burnishing is a time effective process if compared to thermochemical surface treatments such as nitriding that is a time-consuming process and where the compressive residual stresses reach a depth of 0.1 mm for 36 hours of treatment process [63].

4. Conclusions

In this present work, the thermal aspect of the grinding process was studied for different workpiece speeds and cross feed values to optimize its thermal effect on the combined grinding/ball-burnishing process. The ball-burnishing modelling approach based on applying an experimental ball-burnishing force to the burnishing ball is adopted in this study since the modelling approach using a vertical displacement based on Hertz theory of contact is not adequate because it over estimates the indentation depth and further the residual stresses values and profile. This ball-burnishing model chosen in this work was validated numerically and experimentally. Furthermore, the numerical study of the combined grinding/ball-burnishing process was conducted for different friction coefficient values and compared to the experimental study for validation.

In addition, the comparison between combined grinding/ball-burnishing process with the grinding and ball-burnishing processes acting separately permits to see the advantages of the newly developed technique summarized as follows:

- Tensile residual stress obtained after grinding process became compressive thanks to combining grinding/ball-burnishing process acting simultaneously.
- Compressive residual stress results after combined grinding/ball-burnishing process are obtained in both directions and at a more important affected depth than the ball-burnishing process acting separately.
- Combined grinding/ball-burnishing affects a more important workpiece depth (2.7 mm) exceeding the depth obtained by thermo-chemical surface treatments.
- The increase of the burnishing pressure increases the compressive residual stress results and ensures obtaining a deeper compressive layer. The affected depth is stable at a certain pressure threshold value.

A thick layer of the compressive residual stress with small gradient are obtained when grinding and ball-burnishing processes are exerted simultaneously. This might improve workpiece resistance to environmental and mechanical external solicitations like severe rolling contact or slip contact. Future study will focus on investigating the impact of the burnishing pressure, the workpiece speed and the step over on the surface integrity of the simultaneously ground/burnished workpiece.

Acknowledgments: The authors are grateful to the Program "Investissements d'Avenir"-labelled by the French Government and operated by the National Research Agency (ANR) – for financial support to the LabEx MANUTECH-SISE of Université de Lyon (France).

References

1. Mamalis, A. G.; Manolakos, D.; Markopoulos, A. P.; Kundrak, J. Thermal Modelling of Surface Grinding Using Implicit Finite Element Techniques. *Adv. Manuf. Technol.* **2003**, 21, 929–934. doi:10.1007/s00170-002-1410-3
2. Klocke, F.; Brinksmeier, E.; Weinert, K. Capability Profile of Hard Cutting and Grinding Processes. *CIRP Ann. - Manuf. Technol.* **2005**, 54, 22–45. doi:10.1016/S0007-8506(07)60018-3
3. Sanjay, A.; Rao, P.V. Experimental investigation of surface / subsurface damage formation and material removal mechanisms in SiC grinding. *Int. J. Mach. Tools Manuf.* **2008**, 48, 698–710. doi:10.1016/j.ijmachtools.2007.10.013
4. Zhang, J.; Yu, W.; Dong, E.; Zhang, Z.; Jiaxin.S; Gong, G. Study on grinding and deformation fracture control of cold rolled titanium strip. *Metals.* **2020**, 10, 323. doi:10.3390/met10030323
5. Youssef, S.; Ben Salem, W.; Brosse, A.; Hamdi, H. Residual stresses and metallurgic transformations induced by grinding. Int. J. Mach. Mach. Mater. **2011**, 9, 223–232. doi: 10.1504/IJMMM.2011.039648
6. Malkin, S.; Guo, C. Grinding Technology, theory and applications of machining with abrasives.Industrial Press, New York. **2008**, second edition, 1–372, ISBN 978-0-8311-3247-7
7. Malkin, S.; Guo, C. Thermal Analysis of Grinding. *CIRP Ann. - Manuf. Technol.* **2007**, 56, 760–782. doi:10.1016/j.cirp.2007.10.005

8. Wang, Z.; Yu, T.; Wang, X.; Zhang, T.; Zhao, J.; Wen, P.H. Grinding temperature field prediction by meshless finite block method with double infinite element. *Int J Mech Sci*. **2019**, 153–154, 131–142. doi:10.1016/j.ijmecsci.2019.01.037
9. Wenfeng, D.; Jiuhua, X.; Zhenzhen, C.; Honghua, S.; Yucan, F. Grindability and surface integrity of cast nickel-based superalloy in creep feed grinding with brazed CBN abrasive wheels. *Chinese J. Aeronaut.* **2010**, 23, 501–510. doi:10.1016/S1000-9361(09)60247-8
10. Suzuki, S.; Yoshihara, N.; Yan, J. W.; Kuriyagawa, T. High-Efficiency Mirror Grinding of AlN by Ultra-Precision Plane Honing. *Key Eng. Mater.* **2007**, 329, 291–296. doi:10.4028/www.scientific.net/kem.329.291
11. Demir, H.; Gullu, A.; Ciftci, I.; Seker, U. An investigation into the influences of grain size and grinding parameters on surface roughness and grinding forces when grinding. *Stroj. Vestnik/Journal Mech. Eng.* **2010**, 56, 447–454.
12. H. Sallem, H. Hamdi, Analysis of measured and predicted residual stresses by finishing cylindrical grinding of high speed steel with CBN wheel. *Procedia CIRP*. **2015**, 31, 381–386.
13. Mamalis, A. G.; Kundrak, J.; Gyani, K. On the Dry Machining of Steel Surfaces Using Superhard Tools. *Int. J. Adv. Manuf. Technol.* **2002**, 19, 157–162. doi:10.1007/s001700200009
14. Ling, H. ; Yang, C.; Feng, S.; Lu, H. Predictive model of grinding residual stress for linear guideway considering straightening history. *Int J Mech Sci*. **2020**, 176. doi:10.1016/j.ijmecsci. 2020.105536
15. Yang, X.; Richard Liu, C.; Grandt, A. F. An Experimental Study on Fatigue Life Variance, Residual Stress Variance, and Their Correlation of Face-Turned and Ground Ti 6Al-4V Samples. *J. Manuf. Sci. Eng.* **2002**, 124, 809. doi:10.1115/1.1511174
16. Hashimoto, F.; Guo, Y. B.; Warren, A. W. Surface integrity difference between hard turned and ground surfaces and its impact on fatigue life. *CIRP Ann. Manuf. Technol.* **2006**, 55, 81–84. doi:10.1016/S0007-8506(07)60371-0
17. Rajasekaran, B.; Ganesh Sundara Raman, S.; Joshi, S. V.; Sundararajan, G. Effect of grinding on plain fatigue and fretting fatigue behaviour of detonation gun sprayed Cu-Ni-In coating on Al-Mg-Si alloy. *Int. J. Fatigue.* **2009**, 31, 791–796. doi:10.1016/j.ijfatigue.2008.03.003
18. Guo, Y. B.; Warren, A. W.; Hashimoto, F. The basic relationships between residual stress, white layer, and fatigue life of hard turned and ground surfaces in rolling contact. *CIRP J. Manuf. Sci. Technol.* **2010**, 2, 129–134. doi:10.1016/j.cirpj.2009.12.002
19. Xu, R.; Zhou, Y.; Li, X.; Yang, S.; Han, K.; Wang, S. The effect of milling cooling conditions on the surface integrity and fatigue behavior of the GH4169 superalloy. *Metals*. **2019**, 9, 1179. doi:10.3390/met9111179
20. Bouzid Saï, W.; Saï, K. Finite element modeling of burnishing of AISI 1042 steel. *Int. J. Adv. Manuf. Technol.* **2005**, 25, 460–465. doi:10.1007/s00170-003-1993-3
21. Dzierwa, A.; Markopoulos, A. P. Influence of ball-burnishing process on surface topography parameters and tribological properties of hardened steel. *Machines*. **2019**, 7, 11. doi:10.3390/machines7010011
22. Grzesik, W.; Zak, K. Modification of surface finish produced by hard turning using superfinishing and burnishing operations. *J. Mater. Process. Technol.* **2012**, 212, 315–322. doi:10.1016/j.jmatprotec.2011.09.017
23. Zhang, T.; Bugtai, N.; Marinescu, I. D. Burnishing of aerospace alloy: A theoretical-experimental approach. *J. Manuf. Syst.* **2015**, 37, 472–478. doi:10.1016/j.jmsy.2014.11.004

24. Nestler, A.; Schubert, A. Roller burnishing of particle reinforced aluminium matrix composites. *Metals.* **2018**, 8, 95. doi:10.3390/met8020095
25. Dzionk, S.; Scibiorski, B.; Przybylski, W. Surface texture analysis of hardened shafts after ceramic ball burnishing. *Materials.* **2019**, 12, 204. doi:10.3390/ma12020204
26. El-Tayeb, N. S. M.; Low, K. O.; Brevern, P. V. Influence of roller burnishing contact width and burnishing orientation on surface quality and tribological behaviour of Aluminium 6061. *J. Mater. Process. Technol.* **2007**, 186, 272–278. doi:10.1016/j.jmatprotec.2006.12.044
27. Korhonen, H.; Laakkonen, J.; Hakala, J.; Lappalainen, R. Improvements in the surface characteristics of stainless steel workpieces by burnishing with an amorphous diamond-coated tip. *Mach. Sci. Technol.* **2013**, 17, 593–610. doi:10.1080/10910344.2013.837351
28. Revankar, G. D.; Shetty, R.; Rao, S. S.; Gaitonde, V. N. Analysis of surface roughness and hardness in ball burnishing of titanium alloy. *Meas. J. Int. Meas. Confed.* **2014**, 58, 256–268. doi:10.1016/j.measurement.2014.08.043
29. Teimouri, R.; Amini, S. Analytical modeling of ultrasonic surface burnishing process: Evaluation of through depth localized strain. *Int J Mech Sci.* **2019**, 151, 118-132. doi:10.1016/j.ijmecsci.2018.11.008
30. Rodríguez, A.; Calleja, A.; López de Lacalle, L.N.; Pereira, O.; González, H.; Urbikain, G.; Laye, J.;. Burnishing of FSWAluminum Al-Cu-Li components. *Metals.* **2019**, 9, 260. doi:10.3390/met9020260
31. Wierzchowski, D.; Ostertag, A.; Wagner, L. Fatigue Performance of the Mechanically Sur 42CrMo4 and 54SiCr6: Shot Peening vs . Roller-Burnishing. *Icsp.* **2002**, 16–20, 468–473. doi:10.1002/3527606580.ch60
32. Nalla, R. K.; Altenberger, I.; Noster, U.; Liu, G.Y.; Scholtes, B.; Ritchie, R. O. On the influence of mechanical surface treatments-deep rolling and laser shock peening-on the fatigue behavior of Ti-6Al-4V at ambient and elevated temperatures. *Mater. Sci. Eng.* **2003**, 355, 216–230. doi:10.1016/S0921-5093(03)00069-8
33. Majzoobi, G. H.; Zare Jouneghani, F.; Khademi, E. Experimental and numerical studies on the effect of deep rolling on bending fretting fatigue resistance of Al7075. *Int. J. Adv. Manuf. Technol.* **2016**, 82, 2137–2148. doi:10.1007/s00170-015-7542-z
34. Yuan, X.; Li, C. An engineering high cycle fatigue strength prediction model for low plasticity burnished samples. *Int. J. Fatigue.* **2017**, 103, 318–326. doi:10.1016/j.ijfatigue.2017.06.013
35. Fu, H.; Liang, Y. Study of the surface integrity and high cycle fatigue performance of AISI 4340 steel after composite surface modification. *Metals.* **2019**, 9, 856. doi:10.3390/met9080856
36. Maximov, J.; Anchev, A. P. Enhancement of fatigue life of rail-end-bolt holes by slide diamond burnishing. *Eng. Solid Mech.* **2014**, 2, 247–264. doi:10.5267/j.esm.2014.7.001
37. Sanchez, L. E. A.; Giaretta, F.; Nogueira, L. G.; Neto, R. R. I. Effect of Hot Burnishing Aided by Infrared Radiation on the Modification of Surface and Subsurface of AISI 1045 Steel. *Procedia CIRP.* **2017**, 58, 463–468. doi:10.1016/j.procir.2017.03.254
38. Lim, A.; Castagne, S.; Cher, W. C. Effect of Deep Cold Rolling on Residual Stress Distributions Between the Treated and Untreated Regions on Ti – 6Al – 4V Alloy. *J. Manuf. Sci. Eng.* **2017**, 138, 1–8. doi:10.1115/1.4033524
39. Grochała, D.; Berczyński, S.; Grządziel, Z. Modeling of burnishing thermally toughened X42CrMo4 steel with a ceramic ZrO2ball. *Arch. Civ. Mech. Eng.* **2017**, 17, 1011–1018. doi:10.1016/j.acme.2017.04.009
40. Gharbi, F.; Sghaier, S.; Al-Fadhalah; K. J.; Benameur, T. Effect of ball burnishing process on the surface quality and microstructure properties of aisi 1010 steel plates. *J. Mater. Eng. Perform.* **2011**, 20, 903–910. doi:10.1007/s11665-010-9701-6

41. Fu, C. H.; Sealy, M. P.; Guo, Y. B.; Wei, X. T. Austenite-martensite phase transformation of biomedical Nitinol by ball burnishing. *J. Mater. Process. Technol.* **2014**, 214, 3122–3130. doi:10.1016/j.jmatprotec.2014.07.019
42. Balland, P.; Tabourot, L.; Degre, F.; Moreau, V. An investigation of the mechanics of roller burnishing through finite element simulation and experiments. *Int. J. Mach. Tools Manuf.* **2013**, 65, 29–36. doi:10.1016/j.ijmachtools.2012.09.002
43. Hamdi, H.; Zahouani, H.; Bergheau, J. M. Residual stresses computation in a grinding process. *J. Mater. Process. Technol.* **2004**, 147, 277–285. doi:10.1016/S0924-0136(03)00578-8
44. Zhang, Z. Y.*;* Shang, W.; Ding, H. H.; Guo, J.; Wang, H. Y.; Liu, Q. Y.; Wang, W. J. Thermal model and temperature field in rail grinding process based on a moving heat source Thermal model and temperature field in rail grinding process based on a moving heat source. *Appl. Therm. Eng.* **2016**, 106, 855–864. doi:10.1016/j.applthermaleng.2016.06.071
45. Shirsat, U. M.; Ahuja, B. B. Parametric analysis of combined turning and ball burnishing process. *Indian J. Eng. Mater. Sci.* **2004**, 11, 391–396.
46. Mezlini, S.; Mzali, S.; Sghaier, S.; Braham, C.; Kapsa, P. Effect of a combined machining/burnishing tool on the roughness and mechanical properties. *Lubr. Sci.* **2014**, 26, 175–187. doi:10.1002/ls.1239
47. Chaudhari, P.; Awari, G. K.; Khandare, S. S. Investigation of effectiveness of combined turning and burnishing operations performed on lathe machine on an aluminium alloy for the modification of surface texture. *Int. J. of Eng. Sci. Inv. Res. Dev.* **2015**, I, 1316–1320.
48. Rami, A.; Gharbi, F.; Sghaier, S.; Hamdi, H. Some insights on Combined Turning-Burnishing (CoTuB) process on workpiece surface integrity. *Int. J. Precis. Eng. Manuf.* **2018**, 19, 67–78. doi:10.1007/s12541-018-0008-0
49. Kohli, S.; Guo, C.; Malkin, S. Energy Partition to the Workpiece for Grinding with Aluminum Oxide and CBN Abrasive Wheels. *ASME J. Eng. Ind.* **1995**, 117, 160–168. doi:10.1115/1.2803290
50. Li, J.; Li, J. C. M. Temperature distribution in workpiece during scratching and grinding. *Mater. Sci. Eng.* **2005***, A* 409, 108–119. doi:10.1016/j.msea.2005.07.057
51. Xu, X. Experimental study on temperatures and energy partition at the diamond-granite interface in grinding. *Tribol. Int.* **2001**, 34, 419–426. doi:10.1016/S0301-679X(01)00039-1
52. Malkin, S.; Guo, C. Thermal Analysis of Grinding. *CIRP Ann. - Manuf. Technol.* **2007**, 56, 760–782. doi:10.1016/j.cirp.2007.10.005
53. Vinay, P. V; Rao, C. S. Influence of Process Parameters on Grinding - A Review. **2015**.
54. Doman, D. A.; Warkentin, A.; Bauer, R. Finite element modeling approaches in grinding. *Int. J. Mach. Tools Manuf.* **2009**, 49, 109–116. doi:10.1016/j.ijmachtools.2008.10.002
55. Wang, Y.; Chu, X. ; Huang, Y.; Su, G.; Liu, D. Surface residual stress distribution for face gear under grinding with a long-radius disk wheel. *Int J Mech Sci*. **2019**, 159, 260-266. doi:10.1016/j.ijmecsci.2019.06.004
56. Guo, Y. B.; Barkey, M. E. FE-simulation of the effects of machining-induced residual stress profile on rolling contact of hard machined components. *Int. J. Mech. Sci.* **2004**, 46, 371–388. doi:10.1016/j.ijmecsci.2004.03.014
57. Rami, A.; Kallel, A.; Djemaa, S.; Mabrouki, T.; Sghaier, S.; Hamdi, H. Numerical assessment of residual stresses induced by combining turning-burnishing (CoTuB) process of AISI 4140 steel using 3D simulation based on a mixed approach. *Int. J. Adv. Manuf. Technol.* **2018**, 97, 1897–1912. doi:10.1007/s00170-018-2086-7

58. Sartkulvanich, P.; Altan, T.; Jasso, F.; Rodriguez, C. Finite Element Modeling of Hard Roller Burnishing : An Analysis on the Effects of Process Parameters Upon Surface Finish and Residual stresses. *J. Manuf. Sci. Eng.* **2007**, 129, 705–716. doi:10.1115/1.2738121
59. Rami, A.; Kallel, A.; Sghaier, S.; Hamdi, H. Residual stresses computation induced by turning of AISI 4140 steel using 3D simulation based on a mixed approach. Int. J. Adv. Manuf. Technol. **2017**, 91, 3833–3850. doi: 10.1007/s00170-017-0047-1
60. Bhushan, B. *Introduction to tribology*. Wiley. **2002**.
61. Matsumoto, Y.; Magda, D.; Hoeppner, D. W.; Kim, T. Y. Effect of machining processes on the fatigue strength of hardened AISI 4340 steel. *J. Manuf. Sci. Eng. Trans.* **1991***, ASME* 113, 154–159. doi:10.1115/1.2899672
62. Revankar, G. D.; Shetty, R.; Rao, S. S.; Gaitonde, V. N. Wear resistance enhancement of titanium alloy (Ti-6Al-4V) by ball burnishing process. *J. Mater. Res. Technol.* **2017**, 6, 13–32. doi:10.1016/j.jmrt.2016.03.007
63. Ben Fathallah, B.; Dakhli, C. E.; Terres, M. A. The effect of grinding parameters and gas nitriding depth on the grindability and surface integrity of AISI D2 tool steel. *Int. J. Adv. Manuf. Technol.* **2019**, 104, 1449–1459. doi:10.1007/s00170-019-03943-4

Graphical abstract

Yasmine Charfeddine

Experimental set-up

Grinding process

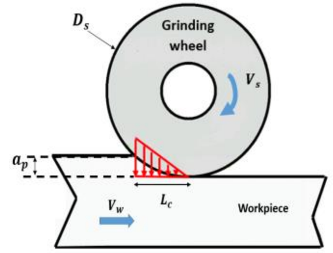

Ball-burnishing process

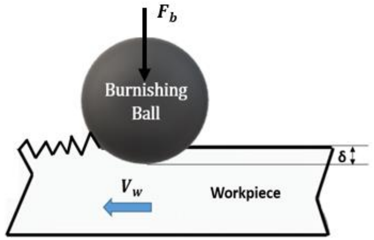

REGAL

Hybrid process

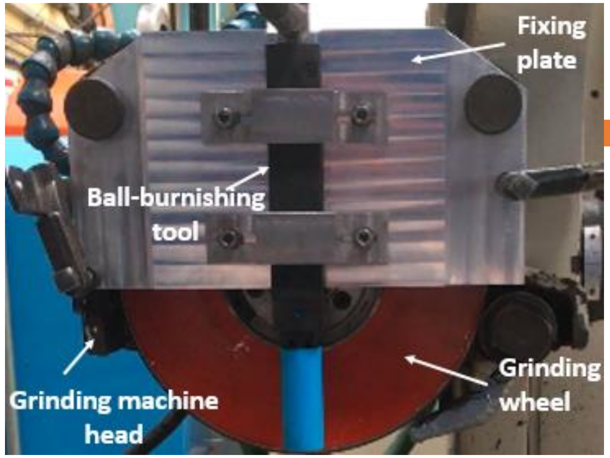

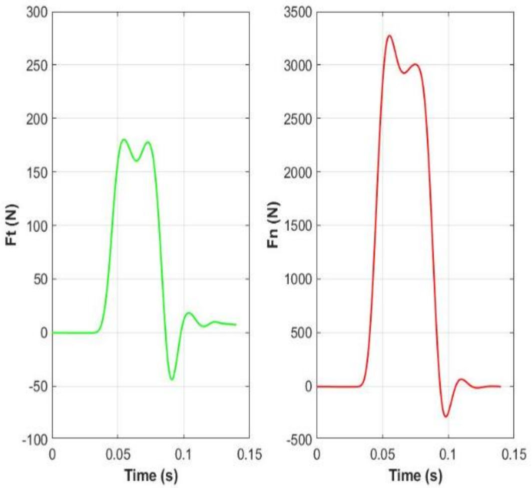

Modelling & 3D FEM simulations

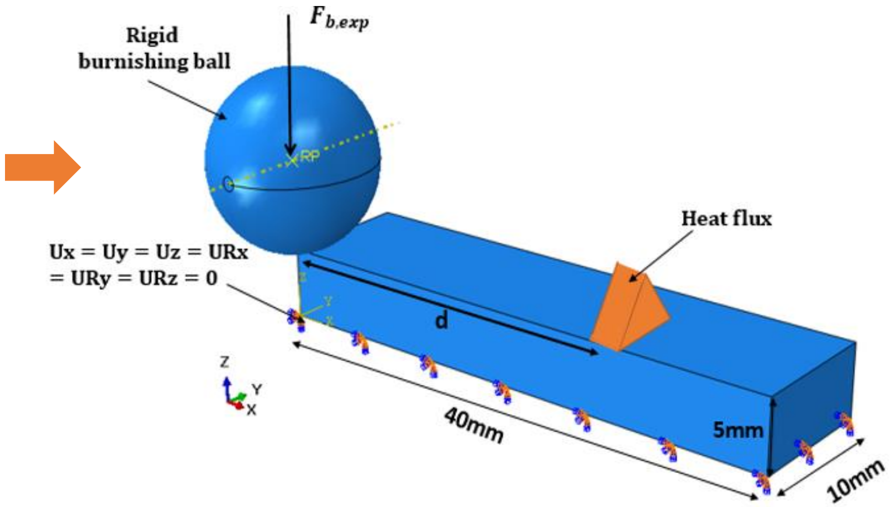

Combined process Grinding/Ball-Burnishing

Experimental REGAL residual stress results vs depth

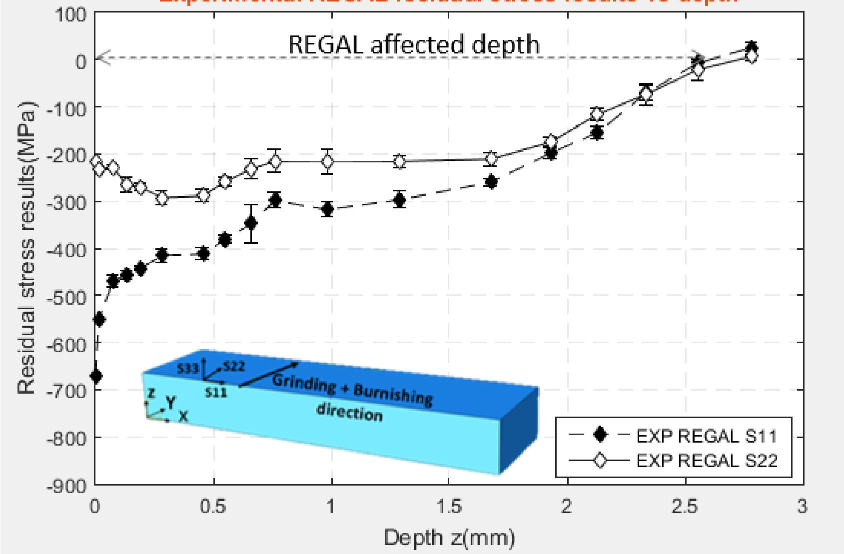

Main results

- Thick Compressive Residual stress layer of about 2.7 mm
- High compressive residual stress level
- A threshold depth is reached for a threshold burnishing force
- Interesting functional surface that may surely improve lifetime in case of severe rolling contact or slip contact, for example

Numerical residual stress results vs depth